Macromolecules

pubs.acs.org/Macromolecules Article

Ultra-Fast Vertical Ordering of Lamellar Block Copolymer Films on Unmodified Substrates

Maninderjeet Singh, Wenjie Wu, Monali N. Basutkar, Joseph Strzalka, Abdullah M. Al-Enizi, Jack F. Douglas, and Alamgir Karim*

Cite This: *Macromolecules* 2021, 54, 1564–1573 Read Online

ACCESS | Metrics & More | Article Recommendations | Supporting Information

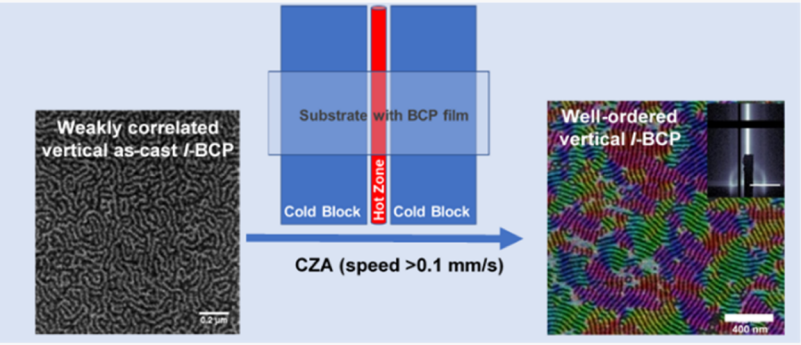

ABSTRACT: To utilize the full potential of block copolymer (BCP) thin films for use in technological devices ranging from ion conduction membranes and transistors to nanowire array antennas, rapid self-assembly of lamellar block copolymers (*l*-BCPs) with vertically oriented lamellar domains on a variety of unmodified substrates is needed. *l*-BCPs have an inherently larger interfacial area for transport compared to their cylindrical counterpart. Our observations demonstrate that the as-cast weakly ordered vertically oriented state of *l*-BCP films of polystyrene-*block*-poly(methyl methacrylate) (PS-*b*-PMMA) from the directional evaporation of select solvents act as "seed templates" for their ultra-fast evolution (≈30 s) into well-ordered vertically oriented nanostructures, using a thermal gradient-based cold zone annealing (CZA) technique. Vertical lamellae are obtained on unmodified substrates, Quartz and Kapton, and the kinetics of *l*-BCP ordering is much faster by CZA as compared to the isotropic oven annealing. The rapid ordering kinetics of vertical *l*-BCPs is tested and found applicable to different molecular masses and film thicknesses ranging from 20 nm to 480 nm, which ultimately flip over to their equilibrium parallel morphology at the upper limits of annealing times. This rapid ordering strategy for the vertical orientation of *l*-BCPs using roll-to-roll compatible CZA would be highly relevant for fundamental studies of interfacial transport as well as for industrial applications from membranes to nanowires.

INTRODUCTION

Block copolymers (BCPs) are a unique class of polymers in which the properties of different types of polymers can be accessed with exceptional structural control at the nanoscale levels.[1,2] Depending on the chemical nature and sizes of the polymer block components, diblock copolymers can phase separate into different morphologies, that is, spherical, cylindrical, gyroid, and lamellar morphologies.[3−5] These morphologies in thin films have a multitude of potential technological applications. For example, spherical and cylindrical morphologies have potential applications in bit-patterned media,[6,7] membranes,[8,9] nanowires arrays,[10] polarizers,[11] and so forth, gyroids have applications for ion conduction channels,[12] whereas lamellar BCPs are potential candidates for nanolithography,[13] dielectric capacitors,[14,15] filtration, and electrolytes in energy storage devices.[16,17]

BCP morphology orientations in thin films can be tuned by using a variety of annealing techniques including thermal annealing,[18] solvent vapor annealing,[19] direct immersion annealing,[20] and so forth. The most widely employed approach for the orientation control of BCPs uses the control of the substrate surface energy.[21] To control the alignment of BCP nanostructures to template structures, directed self-assembly (DSA) is used wherein top-down methods like graphoepitaxy,[22] chemoepitaxy,[23] and so forth direct the BCP nanostructures into the desired orientation. Despite the state-of-the-art control of BCP morphologies, the ordering kinetics in BCPs are usually very slow, that is, hours of annealing times are needed to achieve defect-free orientations. To overcome

Received: August 1, 2020
Revised: October 25, 2020
Published: January 20, 2021

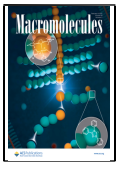

https://dx.doi.org/10.1021/acs.macromol.0c01782
Macromolecules 2021, 54, 1564–1573

the slow ordering kinetics in BCPs, methods such as dynamic thermal gradient-based approaches[51] like cold zone annealing (CZA)[24−27] and laser zone annealing (LZA)[28] have shown a lot of promise. Most of the work in thermal gradient-based approaches have focused on cylindrical BCP (*c*-BCP) systems except for one recent study by Basutkar et al.[29,30] Similar to gradient-based annealing, annealing techniques using temperature ramping over a short period of time such as rapid thermal annealing[31] and microwave annealing[32] have gained popularity over the last decade. This work presents a new dimension of the potential of the dynamic temperature gradient CZA method for the rapid vertical ordering of *l*-BCP films with preset, low-level vertical order from solvent casting.

Applications of BCPs for filtration or ion-conduction membrane require that the connectivity of the channels inside the films should be substantial. In this regard, *l*-BCP provides a high area for filtration or ion conduction[16,33] as compared to most other BCP morphologies. The connectivity of the mechanically robust nonconductive block can provide high mechanical strength while the connectivity of an ion-conductive block in a *l*-BCP provides exceptional control over ionic conduction.[33,34] This unique aspect of *l*-BCP makes them ideal candidates for use as safe and stable solid-state electrolytes in energy storage devices. To enhance the ion conduction in BCP electrolytes compared to homopolymer electrolytes, defect-free and highly interconnected BCP channels are needed. High in-plane conductivities by defect-free BCP channels have been shown;[35] however, creating connected BCP channels throughout the film thickness, especially on unmodified substrates remains challenging. This is because of the differential surface tension of the polymer blocks, which typically results in the higher attraction of one block to the unmodified surfaces as compared to the other, resulting in the layering of polymer blocks in the so-called parallel morphology. Recently, Basutkar et al.[27] demonstrated the vertical orientation of 100 nm thin films of polystyrene-*block*-poly(methyl methacrylate) (PS-*b*-PMMA)-based *l*-BCP on unmodified quartz substrates using a thermal gradient-based CZA technique. The vertical orientation of the *l*-BCP was optimized at a CZA speed of 20 μm/s using a temperature gradient of 48 °C/mm.

In this work, we show ultra-fast vertical ordering (speed (v) > 0.1 mm/s, or annealing time< 40 s) of lamellar PS-*b*-PMMA (*l*-BCPs) having different molecular masses on unmodified substrates [unmodified quartz, polystyrene sulfonate (PSS)-coated quartz, and flexible Kapton] using the thermal gradient-based CZA technique. This is achieved for *l*-BCP films in which the solvent cast state exhibits a weak vertically ordered state with anisotropic block composition fluctuations, set-in by the driving forces of microphase separation via the directional solvent evaporation at the late stages of the film drying process. Such incipient and pre-seeded BCP nuclei structures in solvent cast films have not been explored significantly in any detail with respect to their structural characterization and potential for enhanced DSA-driven long-range ordered BCP structures. We validate our hypothesis that these incipient vertical lamellae seed structures can accelerate the attainment of highly ordered vertical lamellar states with a long-range order and distinct PS and PMMA domain development, by applying CZA, a dynamic thermal gradient-based DSA method. The CZA scanning speeds faster than 0.1 mm/s (>100 μm/s) were used, the highest reported for CZA-S for the ordering of *l*-BCP films. Because of the small difference in surface tension of PS and PMMA and higher in-plane diffusivities as compared to out-of-plane diffusivities,[36] the BCPs maintain the vertical morphology for short annealing times on unmodified substrates. After longer annealing times, the BCPs flip to an equilibrium parallel morphology because of the wetting of the PMMA block on quartz and PS at the air surface. In this window of opportunity of short annealing times explored by high-speed CZA, the initial vertical orientation of the BCP is amplified such that its grain size (ξ) evolution under CZA is much faster ($\xi \approx 98\ t^{0.26}$ nm) than oven annealing ($\xi \approx 75\ t^{0.15}$ nm). Our observation of enhanced ordering kinetics in dynamic gradient-based annealing is consistent with that observed by Berry et al. on the annealing of cylindrical BCPs (*c*-BCP) by CZA.[24] However, the kinetics of *l*-BCP ordering by oven annealing is much slower than that of *c*-BCP as shown by Ruiz et al.,[36] resulting in lower time exponents for grain growth in both CZA and oven annealing of *l*-BCP as compared to *c*-BCP systems. Our study explores the applicability of CZA-induced rapid ordering of weakly correlated vertically oriented as-cast structures over a wide range of film thicknesses in the range of 20 nm (0.6 L_0) to 480 nm (13L_0). We observe that the thinner films (<100 nm) maintain the vertical orientation for shorter times as compared to thicker films, an effect that can be attributed to more pronounced surface wetting effects for thinner films. In films thicker than 4 to 5 L_0 (>150 nm), some meandering of BCP domains from the vertical orientation state in the interior of the film appears in the as-cast state, which decreases with CZA and increases with oven annealing. We show that the vertical orientation by CZA annealing of evaporation-induced vertically ordered as-cast state applies to other low thermal conductivity substrates apart from unmodified quartz as well, that is, water-soluble poly(styrene sulfonate) (PSS)-coated quartz for generating free-standing BCP films by flotation and flexible Kapton substrates for use in flexible electronics. The vertical orientation of pre-seeded BCP films of different thicknesses on quartz, PSS-coated quartz, and Kapton are achievable using an ultra-fast CZA speed of ≈0.2 mm/s.

EXPERIMENTAL SECTION

Materials. Lamellae forming poly(styrene)-*block*-poly(methyl methacrylate) (PS-*b*-PMMA) (molecular masses—33-*b*-33, 19-*b*-17, 45-*b*-44 kg/mol) BCPs were purchased from Polymer source and used without any further purification. The 18% solution of PSS (molecular mass—75 kg/mol) in water was purchased from Sigma-Aldrich. Toluene and tetrahydrofuran (THF) were purchased from VWR and used as received. Silicon substrates were purchased from University Wafers. Quartz substrates (thickness ≈ 0.7 mm) used in this study were purchased from G.M. associates. Flexible Kapton substrates (thickness ≈ 1 mm) were purchased from Dupont.

BCP Film Preparation. The PS-*b*-PMMA BCPs were dissolved in THF or toluene with a mass fraction ranging from 2 wt to 5 wt %. The solutions were flow coated[37] or spin-coated on different substrates. The flow coating speeds or the rpm in the spin-coating were changed to control the film thickness. For annealing (oven or CZA), PS-*b*-PMMA films flow-coated from THF were used. For 19-*b*-17 kg/mol PS-*b*-PMMA, the film thickness studied is around 300 nm, and for 45-*b*-44 kg/mol PS-*b*-PMMA, the film thickness is around 120 nm.

Cold Zone Annealing. The CZA instrument and methodology are described in detail in previous publications.[25,27] A low-resistance (0.025 Ω cm^{-1}) nickel-chrome wire having a diameter of 1 mm insulated by ceramic insulation with an outside diameter of 3.5 mm was used for creating the hot zone. The wire is connected to a high voltage power supply. This hot zone was sandwiched between two aluminum blocks cooled at 10 °C using an ethylene glycol coolant

https://dx.doi.org/10.1021/acs.macromol.0c01782
Macromolecules 2021, 54, 1564−1573

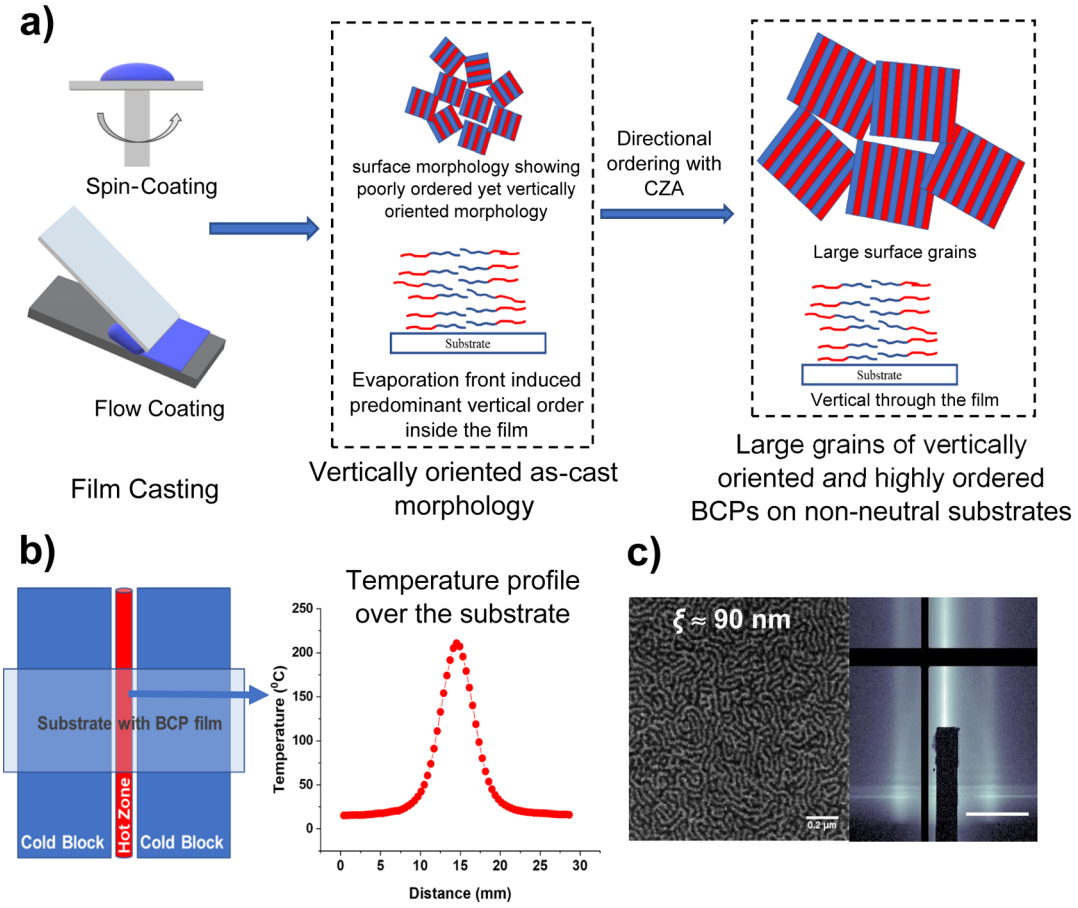

Figure 1. Schematics of the process illustrating the development of the substrate surface independent vertical ordered BCP lamellae by thermal gradient-based CZA technique starting from the poorly ordered yet vertically oriented as-cast state (a) Illustration of evaporation front induced weakly correlated yet vertically oriented BCP nanostructures in as-cast films during film coating. The gain sizes in as-cast films are small (≈2.5 L_0). The in-plane defect annihilation coupled with faster kinetics in CZA produces a highly ordered vertical morphology (b) schematic of CZA setup. The temperature profile shown corresponds to the temperature recorded on the quartz substrate using an IR camera (c) AFM and GISAXS images of as-cast 60 nm PS-*b*-PMMA BCP films flow coated from THF showing a predominant vertical order. Scale bar corresponds to 0.03 $Å^{-1}$ in the GISAXS image.

flowing inside the blocks from a chiller system. Quartz and Kapton substrates have been used for this study owing to their low thermal conductivities (k) (k_{quartz} = 0.14 W m^{-1} K^{-1}, k_{kapton} = 0.37 W m^{-1} K^{-1}). Using a low conductivity substrate helps generate a high thermal gradient on the substrates. The maximum temperature (T_{max}) on the substrate is 210 °C and the temperature gradient (∇T) is ≈50 °C/mm. The CZA annealing times were calculated using the time (t) = distance/CZA speed, where the distance corresponds to the wafer distance having a temperature higher than the glass transition temperature (T_g) on the temperature versus distance profile. The distance for the temperature profile used here corresponds to 4 mm.

Thin-Film Characterization. The topography of BCP films was characterized using a dimension icon atomic force microscopy (AFM) in tapping mode. The through-thickness morphology was characterized by nonselective etching (ablation) using the UV−Ozone etching system and nonsolvent (heptane or water) washing by following the recipe developed by Singh et al.[25] For the characterization of the films on the wafer−film interface, the PSS sacrificial layer was used under the BCP films. Post CZA, the films were floated in water and picked up on a silicon wafer on the reverse side. This allowed the film to be flipped for morphology characterization on the reverse side. The grazing incidence small-angle X-ray scattering (GISAXS) measurements were performed at beamline 8-ID-E of the Advanced Photon Source in Argonne National Lab.[38] An incidence X-ray beam having an energy of 10.9 keV impinged on the BCP film at the angles ranging from 0.10 to 0.16°. At 0.16°, the X-ray beam probes the bulk morphology of the film. For this study, all GISAXS images are shown at 0.16° to supplement the bulk morphology with the surface morphology from AFM. A detector was stationed at a distance of 2185 mm from the sample. Data were collected on a Dectris Pilatus 1M pixel-array detector. Data analysis and conversion to q-space were done using GIXSGUI[39] software in MATLAB, developed at beamline 8-ID-E. The BCP grain sizes were calculated using Scherrer grain size analysis[40] of GISAXS images. The baselines were fit to Intensity versus q profiles and full width at half maximum were used to calculate the grain size. The apparatus resolution, beam divergence, and geometric smearing accounted for less than 3% of the grain size, so these corrections were ignored.

RESULTS AND DISCUSSION

A summary of the CZA approach and illustrative data for the rapid ordering of BCP is shown in Figure 1. We observe that the evaporation fronts during film casting resulted in a poorly ordered yet vertically oriented BCP morphology, independent of the BCP used or the method of film casting (Figure 1c and Supporting Information Figure S1) for BCPs and solvents used in this study. The perpendicular orientation of the cylinder-forming BCPs after the spin-coating has been observed previously for a number of cylinder-forming BCP systems.[41,42] It has been observed in these studies that the formation of micelles in solution results in the vertical orientation of BCP domains upon film casting. Our examination of the as-cast

https://dx.doi.org/10.1021/acs.macromol.0c01782
Macromolecules 2021, 54, 1564−1573

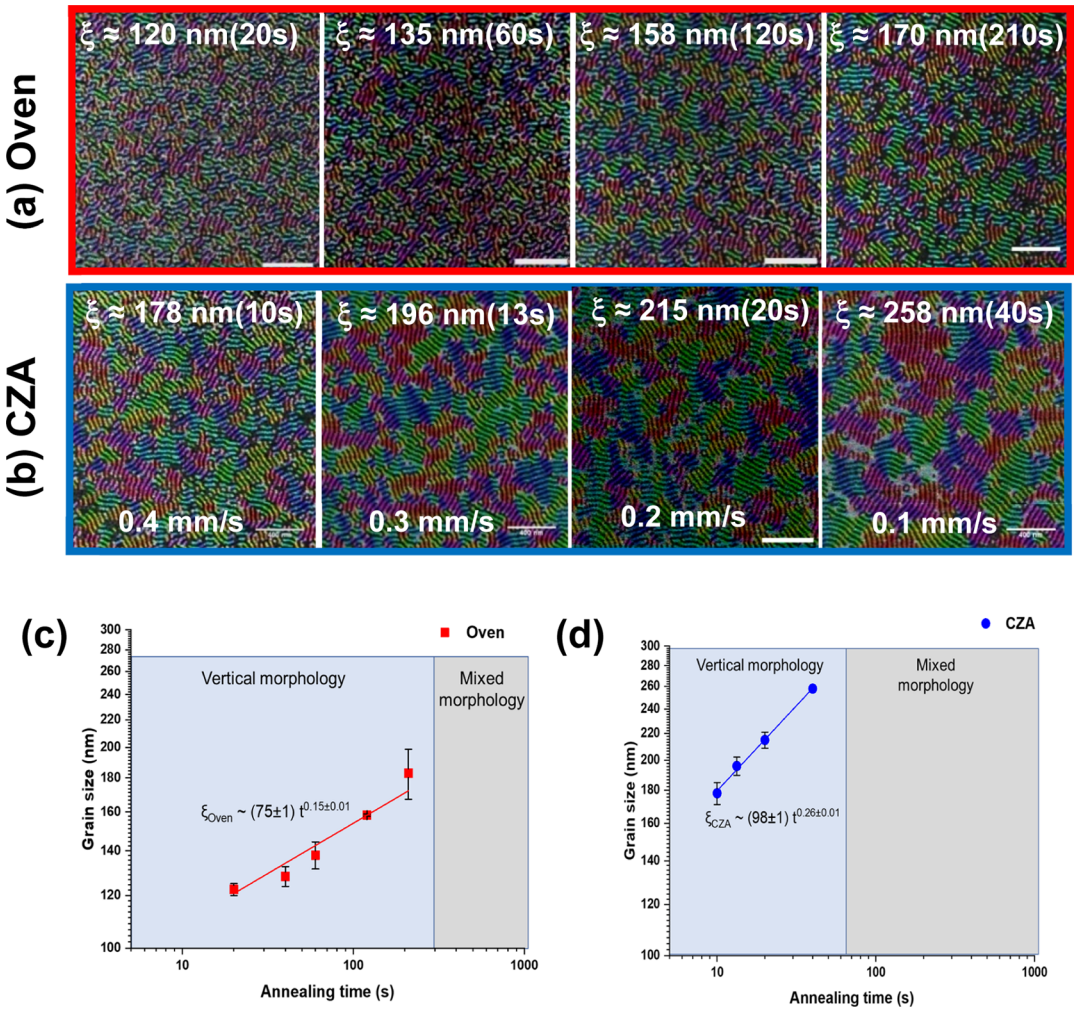

Figure 2. Comparison of BCP ordering during oven annealing with thermal gradient-based annealing (CZA) for a 100 nm thin film. (a) Evolution of grain size (ξ) in oven annealing at different time intervals before flipping to the mixed morphology on nonneutral substrates. (b) Evolution of order in BCP during CZA. CZA speeds are mentioned at the bottom. Images are color-coded to show different orientations of grains. Scale bars correspond to 400 nm in all images in (a,b). (c) Quantitative analysis of the evolution of the grain size in oven annealing shows a time exponent of 0.15 ± 0.01. (d) Time exponent of grain size evolution in CZA is 0.26 ± 0.01, higher than that for the oven annealing as shown in (c). Interestingly, the time taken for BCP to flip to mixed morphology is also faster in CZA indicating faster chain dynamics.

vertical orientation of lamellar BCPs is consistent with the observed orientation effects for cylindrical systems. Figure 1a shows a schematic of the vertical orientation of the BCP film during film casting. Even though the evaporation fronts are able to create mostly a vertical orientation in the as-cast film, the rapid solvent evaporation leaves the as-cast film in a poorly ordered and weakly correlated state. The grain sizes in the as-cast PS-*b*-PMMA film flow coated from THF are close to 2.5 times the BCP domain size ($\xi \approx 2.5\ L_0$) (≈90 nm). The poorly ordered grains at the surface are shown in the schematic along with the predominantly vertically ordered BCP morphology in the bulk. The thermal gradient annealing techniques like CZA,[25] LZA[28] provide directional defect annihilations to perpendicular striped patterns, and hence, lower the activation energy for BCP ordering. Figure 1b shows a sketch of the CZA set up. The temperature gradient is generated on the substrate using a hot wire sandwiched between two cold blocks. The actual temperature profile over the quartz substrate is shown in Figure 1b. The thermal gradient is close to 50 °C/mm and the maximum temperature is 210 °C. Figure 1c shows AFM and GISAXS images of the as-cast PS-*b*-PMMA film flow coated from THF. The vertical orientation of BCP lamellar nanostructures is apparent from AFM as well as GISAXS images. We observed that the THF flow-coated film gives better surface segregation of BCPs, that is, better AFM images, although the BCP film spin-coated or flow coated from other solvents gave similar GISAXS images, indicating a similar degree of the vertical orientation in the bulk of the film (see Supporting Information; Figure S1). The better surface segregation of THF cast films might be because of the faster evaporation of THF and relative neutrality of THF to PS and PMMA blocks as compared to that of toluene. We used THF flow-coated films for further processing given the easy access to the AFM for analysis and comparison of as-cast films to the annealed films. Although we believe that the vertical orientation in the as-cast film is caused by evaporation front, it would be interesting to study how the *l*-BCP films phase separate and order in less than 10 s from the solution state to as-cast films. A further study for the comparison of the effect of the casting solvent or casting methods might be needed for the quantitative comparison of the effect of film casting conditions on as-cast morphologies. Even for non-

https://dx.doi.org/10.1021/acs.macromol.0c01782
Macromolecules 2021, 54, 1564−1573

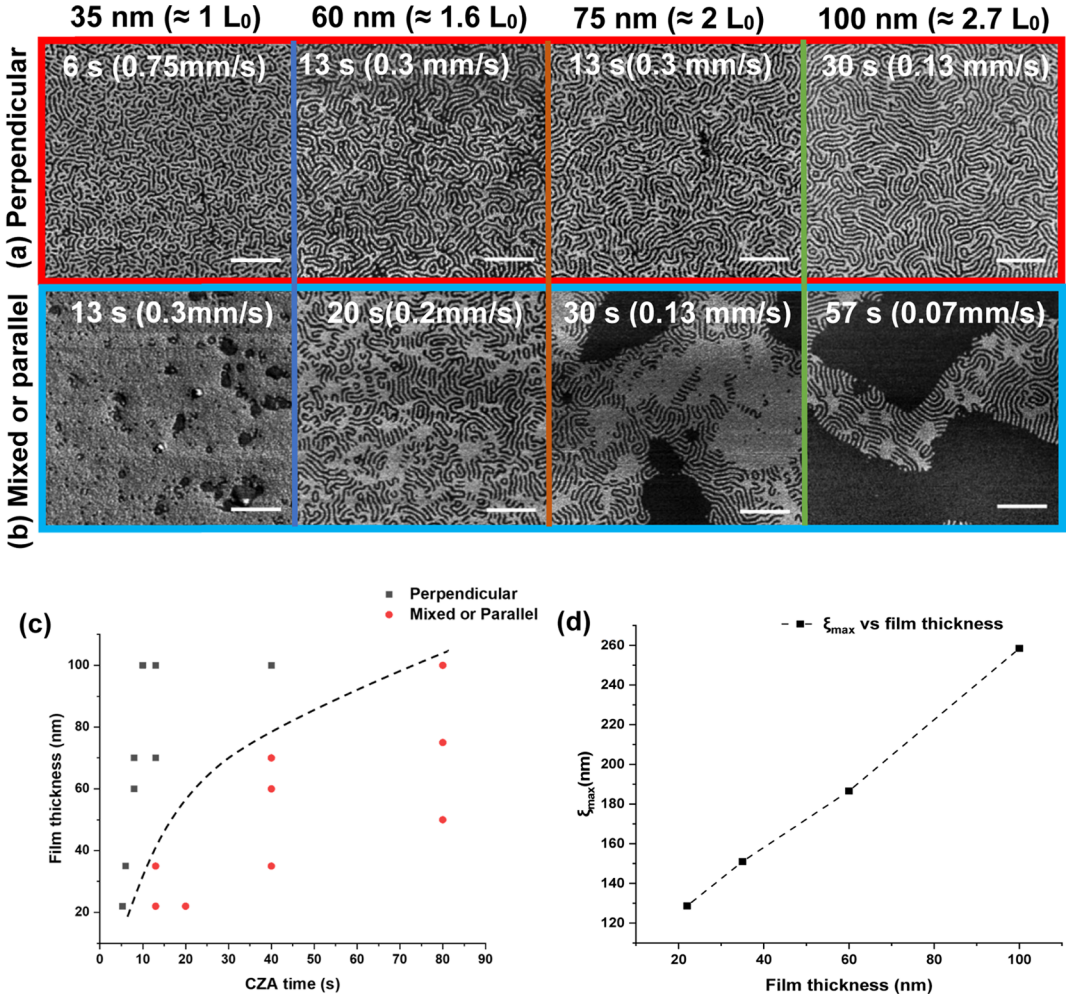

Figure 3. Morphology evolution and morphology diagram showing a BCP orientation as a function of film thickness vs CZA annealing times (and CZA speeds). (a) AFM images showing a perpendicular morphology at different film thicknesses before flipping to mixed morphology. (b) Mixed or parallel BCP morphology [evolved from (a) directly above image] at longer CZA annealing times. Scale bars corresponds to 400 nm in all the images in (a,b). (c) Film thickness vs CZA time morphology diagram of BCP orientation obtained from the AFM images. The dashed line is a guide to the eye. (d) Maximum vertically oriented grain size, that is, grain size right before flipping to the mixed morphology as a function of film thickness. Lines are guides to the eye.

polymeric systems like nanorods[43] or perovskites,[44] solvent evaporation conditions can result in the vertical orientation of nanostructures in the as-cast state, so there may be some universal aspects to the phenomena.

Figure 2 shows the effect of annealing on vertically oriented as-cast BCP films. The effect of widely used oven annealing on 100 nm thin film at an annealing temperature of 210 °C is shown in Figure 2a. Figure 2c shows a quantitative analysis of the short time (t < 5 min) evolution of the grain size (ξ) of vertical lamellae, indicating $\xi \approx 75\ t^{0.15}$ nm. The AFM images are color-coded by the grain orientation and grain sizes. Figure 2b shows the evolution of the vertical grain size during the dynamic thermal gradient-based CZA process. It can be seen that the grain sizes are much larger as compared to oven annealed samples in much lesser time. For comparison, the grain size after CZA annealing for 20 s is around 215 nm, whereas, in oven annealing, the grain size reaches only 170 nm even after annealing for 210 s. Figure 2d shows the kinetic evolution of the grain size during CZA such that $\xi \approx 98\ t^{0.26}$ nm. The grain size (ξ) evolution time exponent is 1.6 times that in oven annealing, and the pre-exponential factor for CZA is higher as compared to that of oven annealing, which shows that lower activation energy is needed for the vertical ordering of *l*-BCP during CZA. The 100 nm film departs from nearly all the vertical to mixed morphology after 5 min of oven annealing at 210 °C because of the preferential interaction between PMMA block having higher surface energy as compared to the PS block[27] and SiO_2 substrate having a surface energy of 74 mJ/m^2.[25] Interestingly, the flipping to mixed morphology for 100 nm film is also faster as compared to oven annealing, as the mixed morphology appears after around 60 s (Figure 2d) as compared to after 300 s in oven annealing. This is because the chain dynamics are also faster in CZA, resulting in a rapid transition to the wetting-driven parallel orientation. It should be pointed out here that two regimes of the ordering of *l*-BCP have been observed in rapid thermal annealing (RTA)[31] on neutral substrates, that is, an initial regime where the time exponent for grain size evolution is 0.29 (close to our CZA observation), followed by a regime having a lower time exponent of 0.05 after about 300 s of annealing.

Different BCP-based applications desire vertically oriented *l*-BCP films across a range of different film thicknesses, for example, the substrate pattern transfer from the BCP films need thinner films ($\approx L_0$) while membrane applications

https://dx.doi.org/10.1021/acs.macromol.0c01782
Macromolecules 2021, 54, 1564−1573

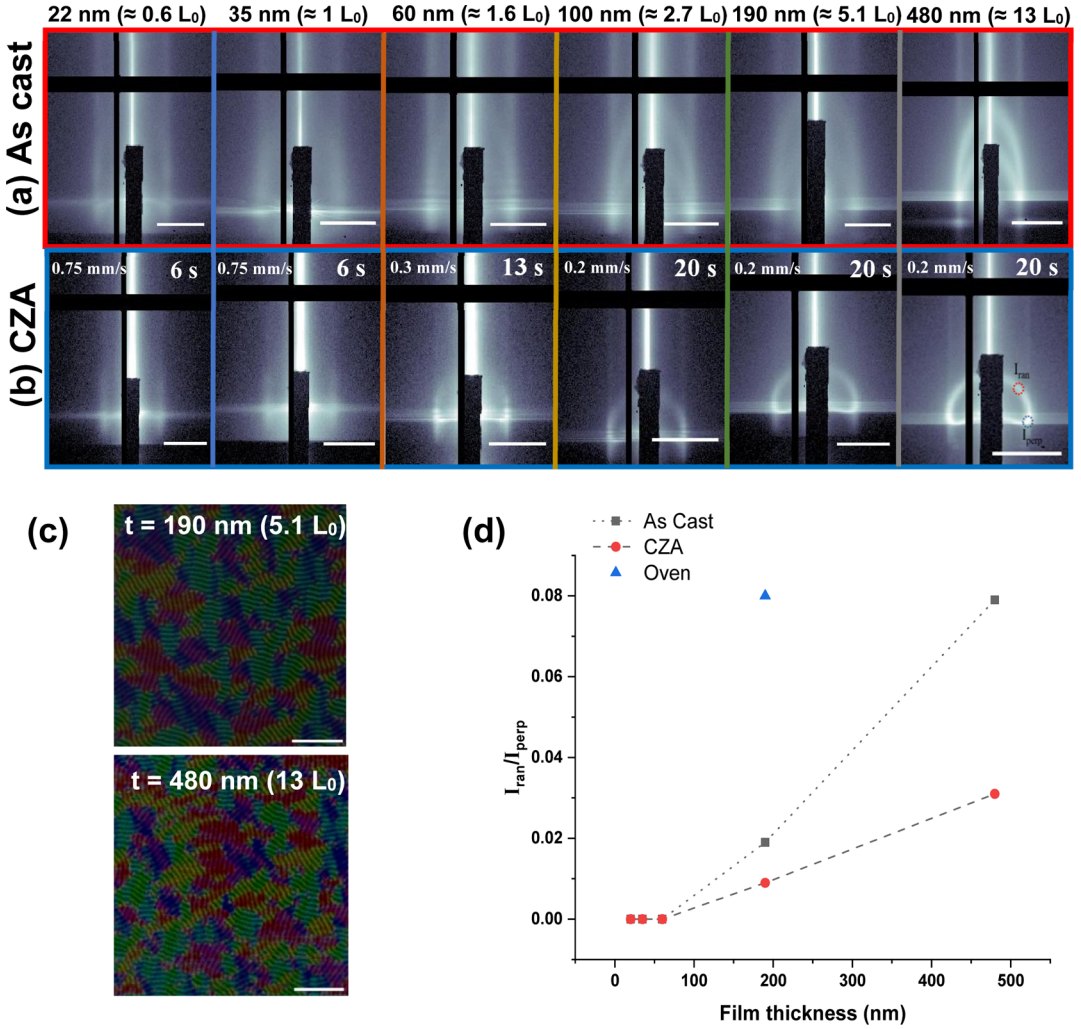

Figure 4. BCP morphology throughout the films as a function of film thickness. (a) GISAXS images (exploring the through-thickness film morphology) showing an increased degree of meandering in as-cast films as a function of film thickness as observed by the appearance of rings. (b) Meandering in as-cast films translates to CZA-annealed films at mentioned times (and CZA speeds). Scale bars correspond to 0.03 $Å^{-1}$ in images in (a,b). (c) AFM images showing a surface perpendicular orientation in thick films processed at 0.2 mm/s CZA speeds. (d) Quantitative analysis of the degree of meandering as a function of film thickness for as-cast, CZA-annealed, and oven-annealed films. I_{ran} and I_{perp} are calculated at points indicated in the 480 nm CZA-annealed films, that is, I_{ran} at 45° and I_{perp} at 0° to the Yoneda band from the center. Lines are guides to the eye.

demand thicker BCP films. We explore the applicability of rapid ordering *l*-BCPs having vertically oriented weakly correlated as-cast structures by CZA to well-ordered nanostructures as a function of film thickness. First, we explore the vertical orientation of films thinner than 100 nm where the substrate wetting effects are dominant.[25] Figure 3 shows the effect of CZA annealing time on the orientation of PS-*b*-PMMA BCP films as a function of film thickness. Figure 3a shows the perpendicular orientation of different film thicknesses at times before flipping to the mixed morphology. It is evident that the thinner films maintain a perpendicular morphology for relatively shorter times as compared to thicker films. Figure 3b shows the mixed morphology of BCP films annealed at relatively longer annealing times. The thinner films transition to the mixed morphology after very short annealing times, while thicker films (>100 nm) take a longer time to transition. A morphology diagram of the BCP orientation is shown in Figure 3c. It has been shown that the substrate effects are dominant in the film thinner than (4−5) L_0,[45] where surface wetting effects driving parallel orientation compete with the CZA-driven vertical domain orientation effects. Additionally, glass transition temperature suppression exists in films thinner than 100 nm, which could be an added factor for the faster flipping of thinner films, coupled with faster kinetics associated with the lower mass of thin films.[46] The activation energy for ordering is inversely related to $T - T_g$, resulting in the availability of more mobility to chains for ordering in films thinner than 100 nm. A similar phenomenon for the faster ordering of thin films was observed by Yager et al., where they found that grain sizes in thinner films on neutral substrates grow faster than the thicker films.[47] Figure 3d shows a plot of the maximum grain size (grain size right before flipping) calculated using GISAXS versus film thickness. Because thinner films flip at very short annealing times, the maximum grain sizes are also smaller for thinner films. Interestingly, the maximum grain size follows the almost linear trend as a function of film thickness.

Figure 4 shows the effect of film thickness on the orientation of as-cast and annealed films using an ultra-fast CZA speed of 0.2 mm/s. Previously, it has been shown that for a cylinder-forming BCP system, films thinner than 100 nm show a parallel orientation after CZA processing at 1 μm/s, and

https://dx.doi.org/10.1021/acs.macromol.0c01782
Macromolecules 2021, 54, 1564−1573

thicker films have a perpendicular morphology along with a surface wetting layer.[25] Given that the activation energy of BCP ordering is lower in thinner films (<100 nm),[48] the thinner films transition to the equilibrium parallel morphology faster than the thicker films. As a result, faster CZA speeds or lower annealing times would be desired to maintain the transient vertical morphology, as shown in Figure 3c. This aspect of maintaining the vertical morphology in sub-100 nm BCP films using faster CZA speeds was not explored by Singh et al.[25] in their study of cylindrical BCPs. As mentioned earlier, the as-cast films have a predominant perpendicular orientation because of locking in of the structure by casting solvent evaporation fronts. We observe that in thin films ($<2L_0$), the evaporation fronts are able to generate a vertical morphology with no mixed or parallel meandering of lamellae as shown by the presence of only vertical streaks in the GISAXS images, as shown in Figure 4a. When the film thickness increases above 3 L_0, hemispherical scattering rings showing meandering lamella of the mixed orientation inside the bulk start appearing in as-cast films. The quantitative analysis of the degree of meandering for as-cast films is shown in Figure 4c. The intensity of rings is less than 10% of the intensity at vertical streaks for film thicknesses studied here, indicating predominantly vertical ordering in as-cast films. The appearance of meandering inside the bulk of the film could be a result of the differential vitrification of the surface and the bulk.[49]

The effect of CZA on BCP ordering as a function of film thickness is shown in Figure 4b. The annealing speeds/effective annealing times are indicated in each of the GISAXS images. The thicker films show highly ordered BCP structures at the surface as indicated by the AFM images shown in Figure 4c. The thicker films show some meandering inside the film as evident by the observation of Debye−Scherrer rings, similar to that observed in as-cast films. This implies that the presence of meandering domains inside thicker films might be correlated to the presence of meandered domains inside the as-cast films. We observe that the fraction of meandering domains versus perpendicular domains is lower in CZA-annealed films as compared to as-cast films, a consequence of the directional defect annihilation nature of CZA. As a qualitative measure, we compare the intensity in the 2-D GISAXS data at a polar angle of 45 ± 2° with the integrated GISAXS intensity at a polar angle of 0° and find that it is less than 5% for the thickest films (≈500 nm) studied here, indicating that the meandering fraction of the film is much smaller than the vertically oriented fraction of the film.

To supplement the GISAXS characterization for through film morphology, we characterized the BCP morphology throughout the film thickness by ablation test and by AFM characterization on the reverse side of the film. For the ablation of the films, we used a method developed by Singh at al.[25] The films were etched using ozone created inside an ultraviolet (UV) radiation chamber and washed with a nonsolvent (heptane or water). The AFM was performed post-ablation to characterize the BCP morphology. Figure S2 (Supporting Information) shows the morphology of 100 nm (CZA speeds ~0.11 to 0.13 mm/s) after ultraviolet ozone (UVO) ablation at different film thicknesses. The vertical orientation throughout the film is apparent from the AFM images shown in Figure S2. We characterized a ≈280 nm film after picking it up on the silicon wafer on the reverse side after floating (in water) the CZA processed (speed ≈0.2 mm/s) BCP film from the PSS-coated quartz substrates. Figure S3 shows the AFM height images of the BCP films picked on the reverse side. The film shows a mostly parallel or meandered morphology, as shown in Figure S3a. After etching the reverse picked film for ≈35 nm, the vertical morphology appears as shown in Figure S3b. This shows that the thicker BCP films have a predominantly meandered or parallel surface layer and the rest of the films have a vertical morphology. The Debye−Scherrer rings observed in the CZA processed thicker films, as shown in Figure 4, might be because of this surface meandered layer, and as a result, the intensity due to vertical orientation is much higher than the intensity due to the meandered morphology.

The comparison of meandered fraction in oven annealing as compared to CZA and as-cast films is also shown in Figure 4c for a film thickness of 190 nm. The oven-annealed films show a much higher degree of meandering, that is, close to 8% as compared to 2% in the as-cast state and 1% in CZA-annealed films. We believe that these numbers should be used for the qualitative comparison between different annealing methods rather than being used as an actual degree of meandering in the films. The nondirectional nature of oven annealing makes substrate wetting effects more dominating, thus resulting in a higher degree of meandering. On the other hand, the directional annealing nature in CZA coupled with faster dynamics and short annealing times helps in attaining a minimum degree of meandering in CZA-annealed films.

Furthermore, we achieve the vertical BCP ordering on low conductivity flexible substrates like Kapton and quartz substrates having a sacrificial polymer layer of PSS, which is soluble in polar solvents like water and insoluble in nonpolar solvents like toluene used for film casting of PS-*b*-PMMA The sacrificial layer allows floating the ordered BCP films to produce free-standing BCP membranes, potentially useful for ion conduction or filtration applications. Figure 5a shows the ordered PS-*b*-PMMA lamellar nanostructures (thickness ≈ 300 nm) on the PSS sacrificial layer by using CZA (speed ≈ 0.2 mm/s) within 20 s of ordering by annealing. This shows that the BCP ordering can be achieved on chemically modified substrates by the as-cast vertical orientation and in-plane defect annihilation by CZA. For the use of the BCP nanostructure for applications in flexible electronics and roll-to-roll fabrication at an industrial scale, the use of flexible substrates is pertinent. Figure 5b shows the vertically oriented BCP lamellae on highly flexible 1 mm thick Kapton substrates without any surface modification.

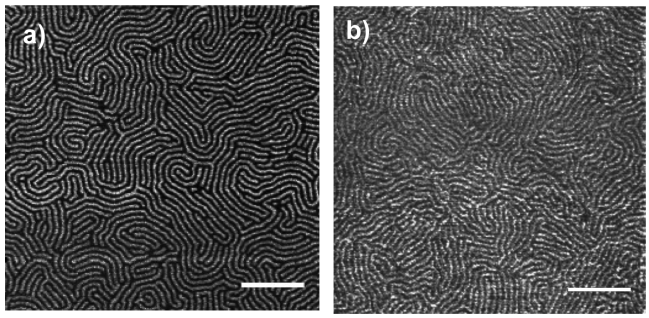

Figure 5. Vertical orientation of BCP lamellae on (a) sacrificial PSS layer on quartz substrate (b) flexible Kapton substrate using a CZA speed of 0.2 mm/s. Scale bar corresponds to 400 nm in both images.

For different applications of BCPs, a range of BCP domain sizes with a controlled orientation might be desired. For

https://dx.doi.org/10.1021/acs.macromol.0c01782
Macromolecules 2021, 54, 1564−1573

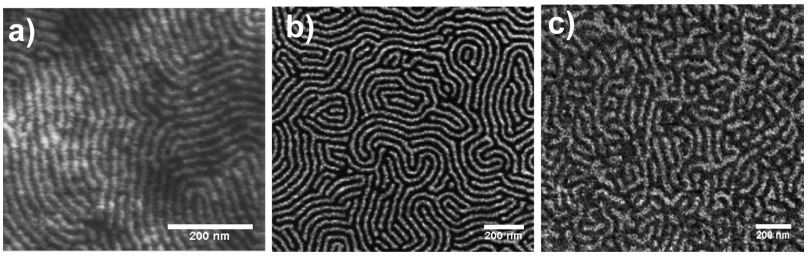

Figure 6. Efficacy of CZA to produce vertically oriented lamellar BCP nanostructures for different molecular masses (M_w) BCPs (a) vertically oriented *l*-BCP with M_w 19-*b*-17 kg/mol. (b) Vertically oriented *l*-BCP with M_w 33-*b*-33 kg/mol. (c) Vertically oriented *l*-BCP with M_w 45-*b*-44 kg/mol. All three films are processed using CZA at a speed of 0.2 mm/s. The scale bar corresponds to 200 nm in all three images.

example, it has been observed that the normalized ionic conductivity of BCP electrolytes has a strong dependence on the BCP molecular mass (domain size).[50] Similarly, different filtration applications demand tunable channel lengths for the filtration of solute particles having different sizes. Furthermore, given that the viscosity and the segregation strength of the BCPs is a strong function of the molecular mass, it is pertinent to test the applicability of rapid CZA for controlling the BCP orientation across different molecular masses. In this study, we have studied the PS-*b*-PMMA orientation and kinetics using a molecular mass of 33-*b*-33 kg/mol, as shown in Figures 2−5. Now, we examine the orientation of PS-*b*-PMMA with molecular masses of 19-*b*-17 kg/mol and 45-*b*-44 kg/mol after rapid CZA processing at a speed of 0.2 mm/s. As shown in Figure 6, 19-*b*-17 kg/mol, 33-*b*-33 kg/mol, and 45-*b*-44 kg/mol PS-*b*-PMMA BCPs show a vertical orientation on Quartz substrates post CZA processing. The thicknesses of 19-*b*-17 kg/mol, 33-*b*-33 kg/mol, and 45-*b*-44 kg/mol are 300 nm, 190 nm, and 120 nm respectively, for the data shown in Figure 6. Furthermore, we can qualitatively observe that the grain size in 45-*b*-44 kg/mol PS-*b*-PMMA is smaller than that in 33-*b*-33 kg/mol and 19-*b*-17 kg/mol PS-*b*-PMMA BCP after CZA processing. This is expected because the viscosity of BCPs increases with increasing the molecular mass, thereby increasing the activation energy of ordering in higher molecular mass BCPs. The vertical orientation of different molecular mass BCPs (19-*b*-17, 33-*b*-33, 45-*b*-44 kg/mol) using rapid CZA processing opens avenues for the use of CZA as a processing method for controlling the BCP orientation with tunable domain spacings.

CONCLUSIONS

We have shown the rapid fabrication of vertically oriented PS-*b*-PMMA *l*-BCPs on unmodified substrates using thermal dynamic gradient-based CZA in less than 40 s using CZA speeds faster than 0.1 mm/s. The evaporation front-induced poorly ordered vertical phase separation was driven into highly ordered, vertical morphology lamellae on directional annealing with CZA. The grain size follows $\xi \approx 98\ t^{0.26}$ nm in CZA as compared to $\xi \approx 75\ t^{0.15}$ nm in oven annealing, indicating the faster kinetics of *l*-BCP ordering in CZA, resulting in the also shorter time taken to flip to the parallel morphology. We have constructed a film thickness vs annealing time morphology diagram for CZA, which shows that thinner films (<100 nm) maintain the vertical orientation for shorter times, probably because of lower glass transition temperatures or wetting effects. The maximum grain size is also lower in thinner films because of shorter annealing times for maintaining the vertical morphology. For thicker films [$h > (4-5)\ L_0$], the meandering fraction appears in the as-cast morphology, but the meandering fraction decreases in directional CZA-processed films and increases in isotropic oven-annealed films, as compared to as-cast films. The generality of the evaporation-induced as-cast vertical orientation and CZA-induced high degree of ordering has been shown with BCPs on a sacrificial layer and on a flexible Kapton substrate. We show that the vertical orientation using the rapid CZA is applicable to different molecular masses as well. Our findings may pave the way for use of BCP to rapidly fabricate nanostructures on a variety of substrates in a single annealing step.

ASSOCIATED CONTENT

Supporting Information

The Supporting Information is available free of charge at https://pubs.acs.org/doi/10.1021/acs.macromol.0c01782.

Vertical orientation of PS-*b*-PMMA in the as-cast state from different solvents, ablation tests, and flip tests to characterize the through thickness BCP morphology (PDF)

AUTHOR INFORMATION

Corresponding Author

Alamgir Karim − *Department of Chemical and Biomolecular Engineering, University of Houston, Houston, Texas 77204, United States;* orcid.org/0000-0003-1302-9374; Email: akarim3@central.uh.edu

Authors

Maninderjeet Singh − *Department of Chemical and Biomolecular Engineering, University of Houston, Houston, Texas 77204, United States*

Wenjie Wu − *Department of Chemical and Biomolecular Engineering, University of Houston, Houston, Texas 77204, United States*

Monali N. Basutkar − *Department of Polymer Engineering, University of Akron, Akron, Ohio 44325, United States;* orcid.org/0000-0002-5920-2104

Joseph Strzalka − *X-Ray Science Division, Argonne National Laboratory, Argonne, Illinois 60439, United States;* orcid.org/0000-0003-4619-8932

Abdullah M. Al-Enizi − *Department of Chemistry, College of Science, King Saud University, Riyadh 11451, Saudi Arabia;* orcid.org/0000-0002-3967-5553

Jack F. Douglas − *Material Science and Engineering Division, National Institute of Standards and Technology (NIST), Gaithersburg, Maryland 20899, United States;* orcid.org/0000-0001-7290-2300

Complete contact information is available at: https://pubs.acs.org/10.1021/acs.macromol.0c01782

https://dx.doi.org/10.1021/acs.macromol.0c01782
Macromolecules 2021, 54, 1564−1573

Notes

Certain commercial equipment, instruments, or materials are identified in this paper in order to specify the experimental procedure accurately. Such identification is not intended to imply recommendation or endorsement by the National Institute of Standards and Technology, nor is it intended to imply that the materials or equipment identified are necessarily the best available for the purpose.

The authors declare no competing financial interest.

■ ACKNOWLEDGMENTS

We thank NSF-DMR 1905996 for partial funding related to the project. The authors also extend their sincere appreciation to Researchers Supporting Project number (RSP-2020/55), King Saud University, Riyadh, Saudi Arabia for partially funding of this research. The authors acknowledge the use of resources of the Advanced Photon Source, a U.S. Department of Energy (DOE) Office of Science User Facility operated for the DOE Office of Science by Argonne National Laboratory under Contract no. DE-AC02-06CH11357.

■ REFERENCES

(1) Epps, T. H., III; O'Reilly, R. K. Block copolymers: Controlling nanostructure to generate functional materials - Synthesis, characterization, and engineering. *Chem. Sci.* **2016**, *7*, 1674−1689.
(2) Mai, Y.; Eisenberg, A. Self-assembly of block copolymers. *Chem. Soc. Rev.* **2012**, *41*, 5969−5985.
(3) Hu, H.; Gopinadhan, M.; Osuji, C. O. Directed self-Assembly of block copolymers: A tutorial review of strategies for enabling nanotechnology with soft matter. *Soft Matter* **2014**, *10*, 3867−3889.
(4) Bang, J.; Jeong, U.; Ryu, D. Y.; Russell, T. P.; Hawker, C. J. Block copolymer nanolithography: Translation of molecular level control to nanoscale patterns. *Adv. Mater.* **2009**, *21*, 4769−4792.
(5) Hamley, I. W. Ordering in thin films of block copolymers: Fundamentals to potential applications. *Prog. Polym. Sci.* **2009**, *34*, 1161−1210.
(6) Segalman, R. A. Patterning with block copolymer thin films. *Mater. Sci. Eng., R* **2005**, *48*, 191−226.
(7) Cummins, C.; Ghoshal, T.; Holmes, J. D.; Morris, M. A. Strategies for Inorganic Incorporation using Neat Block Copolymer Thin Films for Etch Mask Function and Nanotechnological Application. *Adv. Mater.* **2016**, *28*, 5586−5618.
(8) Phillip, W. A.; O'Neill, B.; Rodwogin, M.; Hillmyer, M. A.; Cussler, E. L. Self-assembled block copolymer thin films as water filtration membranes. *ACS Appl. Mater. Interfaces* **2010**, *2*, 847−853.
(9) Luo, Y.; et al. Vertically oriented nanoporous block copolymer membranes for oil/water separation and filtration. *Soft Matter* **2020**, *16*, 9648.
(10) Majewski, P. W.; Rahman, A.; Black, C. T.; Yager, K. G. Arbitrary lattice symmetries via block copolymer nanomeshes. *Nat. Commun.* **2015**, *6*, 7448.
(11) Kim, S. Y.; Gwyther, J.; Manners, I.; Chaikin, P. M.; Register, R. A. Metal-containing block copolymer thin films yield wire grid polarizers with high aspect ratio. *Adv. Mater.* **2014**, *26*, 791−795.
(12) Werner, J. G.; Rodríguez-Calero, G. G.; Abruña, H. D.; Wiesner, U. Block copolymer derived 3-D interpenetrating multifunctional gyroidal nanohybrids for electrical energy storage. *Energy Environ. Sci.* **2018**, *11*, 1261−1270.
(13) Bates, C. M.; Maher, M. J.; Janes, D. W.; Ellison, C. J.; Willson, C. G. Block copolymer lithography. *Macromolecules* **2014**, *47*, 2−12.
(14) Samant, S. P.; et al. Directed Self-Assembly of Block Copolymers for High Breakdown Strength Polymer Film Capacitors. *ACS Appl. Mater. Interfaces* **2016**, *8*, 7966−7976.
(15) Samant, S.; et al. Effect of Molecular Weight and Layer Thickness on the Dielectric Breakdown Strength of Neat and Homopolymer Swollen Lamellar Block Copolymer Films. *ACS Appl. Polym. Mater.* **2020**, *2*, 3072−3083.
(16) Liu, T.; Liu, G. Block copolymers for supercapacitors, dielectric capacitors and batteries. *J. Phys.: Condens. Matter* **2019**, *31*, 233001.
(17) Young, W.-S.; Kuan, W.-F.; Epps, T. H. Block copolymer electrolytes for rechargeable lithium batteries. *J. Polym. Sci., Part B: Polym. Phys.* **2014**, *52*, 1−16.
(18) Ruiz, R.; et al. Density Multiplication and Improved Copolymer Assembly. *Science* **2008**, *321*, 936−939.
(19) Sinturel, C.; Vayer, M.; Morris, M.; Hillmyer, M. A. Solvent vapor annealing of block polymer thin films. *Macromolecules* **2013**, *46*, 5399−5415.
(20) Modi, A.; et al. Direct Immersion Annealing of Thin Block Copolymer Films. *ACS Appl. Mater. Interfaces* **2015**, *7*, 21639−21645.
(21) Mansky, P.; Liu, Y.; Huang, E.; Russell, T. P.; Hawker, C. Controlling Polymer-Surface Interactions with Random Copolymer Brushes. *Science* **1997**, *275*, 1458−1460.
(22) Segalman, R. A.; Yokoyama, H.; Kramer, E. J. Graphoepitaxy of spherical domain block copolymer films. *Adv. Mater.* **2001**, *13*, 1152−1155.
(23) Kim, S. O.; et al. Epitaxial self-assembly of block copolymers on lithographically defined nanopatterned substrates. *Nature* **2003**, *424*, 411−4.
(24) Berry, B. C.; Bosse, A. W.; Douglas, J. F.; Jones, R. L.; Karim, A. Orientational order in block copolymer films zone annealed below the order-disorder transition temperature. *Nano Lett.* **2007**, *7*, 2789−2794.
(25) Singh, G.; et al. Tuning molecular relaxation for vertical orientation in cylindrical block copolymer films via sharp dynamic zone annealing. *Macromolecules* **2012**, *45*, 7107−7117.
(26) Singh, G.; Yager, K. G.; Berry, B.; Kim, H.-C.; Karim, A. Dynamic thermal field-induced gradient soft-shear for highly oriented block copolymer thin films. *ACS Nano* **2012**, *6*, 10335−10342.
(27) Basutkar, M. N.; et al. Through-Thickness Vertically Ordered Lamellar Block Copolymer Thin Films on Unmodified Quartz with Cold Zone Annealing. *Nano Lett.* **2017**, *17*, 7814−7823.
(28) Majewski, P. W.; Yager, K. G. Millisecond Ordering of Block Copolymer Films via Photothermal Gradients. *ACS Nano* **2015**, *9*, 3896−3906.
(29) Basutkar, M. N.; et al. Aligned Morphologies in Near-Edge Regions of Block Copolymer Thin Films. *Macromolecules* **2019**, *52*, 7224−7233.
(30) Samant, S.; et al. Ordering pathway of block copolymers under dynamic thermal gradients studied by in situ GISAXS. *Macromolecules* **2016**, *49*, 8633−8642.
(31) Ferrarese Lupi, F.; et al. Rapid thermal processing of self-assembling block copolymer thin films. *Nanotechnology* **2013**, *24*, 315601.
(32) Zhang, X.; Harris, K. D.; Wu, N. L. Y.; Murphy, J. N.; Buriak, J. M. Fast assembly of ordered block copolymer nanostructures through microwave annealing. *ACS Nano* **2010**, *4*, 7021−7029.
(33) Hallinan, D. T.; Balsara, N. P. Polymer Electrolytes. *Annu. Rev. Mater. Res.* **2013**, *43*, 503−525.
(34) Gwee, L.; Choi, J.-H.; Winey, K. I.; Elabd, Y. A. Block copolymer/ionic liquid films: The effect of ionic liquid composition on morphology and ion conduction. *Polymer* **2010**, *51*, 5516−5524.
(35) Kambe, Y.; et al. Role of Defects in Ion Transport in Block Copolymer Electrolytes. *Nano Lett.* **2019**, *19*, 4684−4691.
(36) Ruiz, R.; Sandstrom, R. L.; Black, C. T. Induced orientational order in symmetric diblock copolymer thin films. *Adv. Mater.* **2007**, *19*, 587−591.
(37) Stafford, C. M.; Roskov, K. E.; Epps, T. H.; Fasolka, M. J. Generating thickness gradients of thin polymer films via flow coating. *Rev. Sci. Instrum.* **2006**, *77*, 023908.
(38) Jiang, Z.; et al. The dedicated high-resolution grazing-incidence X-ray scattering beamline 8-ID-E at the Advanced Photon Source. *J. Synchrotron Radiat.* **2012**, *19*, 627−636.
(39) Jiang, Z. GIXSGUI: a MATLAB toolbox for grazing-incidence X-ray scattering data visualization and reduction, and indexing of buried three-dimensional periodic nanostructured films. *J. Appl. Crystallogr.* **2015**, *48*, 917−926.

https://dx.doi.org/10.1021/acs.macromol.0c01782
Macromolecules 2021, 54, 1564−1573

(40) Smilgies, D.-M. Scherrer grain-size analysis adapted to grazing-incidence scattering with area detectors. *J. Appl. Crystallogr.* **2009**, *42*, 1030−1034.
(41) Lin, Z. Q.; Boosahda, L.; Stone, D.; Larose, L.; Russell, T. P. A Rapid Route to Arrays of Nanostructures in Thin Films. *Adv. Mater.* **2002**, *14*, 1373−1376.
(42) Park, S.; Wang, J.-Y.; Kim, B.; Chen, W.; Russell, T. P. Solvent-induced transition from micelles in solution to cylindrical micro-domains in diblock copolymer thin films. *Macromolecules* **2007**, *40*, 9059−9063.
(43) Baker, J. L.; Widmer-Cooper, A.; Toney, M. F.; Geissler, P. L.; Alivisatos, A. P. Device-scale perpendicular alignment of colloidal nanorods. *Nano Lett.* **2010**, *10*, 195−201.
(44) Soe, C. M. M.; et al. Understanding Film Formation Morphology and Orientation in High Member 2D Ruddlesden−Popper Perovskites for High-Efficiency Solar Cells. *Adv. Energy Mater.* **2018**, *8*, 1700979.
(45) Albert, J. N. L.; Epps, T. H. Self-assembly of block copolymer thin films. *Mater. Today* **2010**, *13*, 24−33.
(46) Young, R. J.; Lovell, P. A. *Introduction to Polymers*, 3rd ed.; CRC Press, Taylor & Francis Group, 2010.
(47) Black, C. T.; Forrey, C.; Yager, K. G. Thickness-dependence of block copolymer coarsening kinetics. *Soft Matter* **2017**, *13*, 3275−3283.
(48) Doerk, G. S.; Li, R.; Fukuto, M.; Rodriguez, A.; Yager, K. G. Thickness-Dependent Ordering Kinetics in Cylindrical Block Copolymer/Homopolymer Ternary Blends. *Macromolecules* **2018**, *51*, 10259−10270.
(49) Zhang, X.; et al. Surface Morphology Diagram for Cylinder-Forming Block Copolymer Thin Films. *ACS Nano* **2008**, *2*, 2331−2341.
(50) Yuan, R.; et al. Ionic Conductivity of Low Molecular Weight Block Copolymer Electrolytes. *Macromolecules* **2013**, *46*, 914−921.
(51) Singh, M.; Basutkar, M.; Samant, S.; Singh, G.; Karim, A. Directed Self-assembly of Block Copolymers with Dynamic Thermal Gradients. *Soft Matter and Biomaterials on the Nanoscale*; World Scientific, 2020; Chapter 9, pp 373−409.

https://dx.doi.org/10.1021/acs.macromol.0c01782
Macromolecules 2021, 54, 1564−1573